Low-cost MRI devices and methods for real-time monitoring of flow and transfer phenomena in milli-channels

Feryal Guerroudj, Laouès Guendouz, Rainier Hreiz, Jean-Marc Commenge, Lucie Klopffer, Nicolas Louvet, Laurence Mathieu, Jean-Christophe Perrin

▶ **To cite this version:**

Feryal Guerroudj, Laouès Guendouz, Rainier Hreiz, Jean-Marc Commenge, Lucie Klopffer, et al.. Low-cost MRI devices and methods for real-time monitoring of flow and transfer phenomena in milli-channels. Italian-French International Conference on Magnetic Resonance, Sep 2022, Milan, Italy. 10.1515/pac-2023-0105 . hal-04137362

HAL Id: hal-04137362
https://hal.science/hal-04137362

Submitted on 22 Jun 2023

HAL is a multi-disciplinary open access archive for the deposit and dissemination of scientific research documents, whether they are published or not. The documents may come from teaching and research institutions in France or abroad, or from public or private research centers.

L'archive ouverte pluridisciplinaire **HAL**, est destinée au dépôt et à la diffusion de documents scientifiques de niveau recherche, publiés ou non, émanant des établissements d'enseignement et de recherche français ou étrangers, des laboratoires publics ou privés.

Conference paper

Feryal Guerroudj, Laouès Guendouz, Rainier Hreiz, Jean-Marc Commenge, Lucie Klopffer, Nicolas Louvet, Laurence Mathieu and Jean-Christophe Perrin*

Low-cost MRI devices and methods for real-time monitoring of flow and transfer phenomena in milli-channels

https://doi.org/10.1515/pac-2023-0105

Abstract: An NMR/MRI methodology is developed for the study of flows in miniaturized systems handling volumes of fluid in the microliter range. Specific MRI devices are implemented, including radiofrequency coils with millimetric dimensions whose size and geometry correspond to the studied systems. We follow a low-cost development procedure of home-made milli-RF coils, including their dimensioning, the simulation of the produced electromagnetic field, their fabrication and their integration in experimental devices. In each of the two cases presented the filling factor is optimized and the sensitivity of the measurement is greatly improved over standard commercial instrumentations by a factor up to 17. Two applications are then discussed: the characterization of the hydrodynamics in an anchor shaped micromixer and the monitoring of the development of a biofilm at the pore scale.

Keywords: Biofilms; micromixers; milli-fluidics; NMR; NMR/MRI methods; radiofrequency milli-RF coils.

Introduction

Milli-fluidics is the science and the technology of flows in systems with characteristic dimensions of a few hundred microns [1]. These systems are developed and used with an increasing success in chemical and biological sciences [2, 3] and in process engineering [4], presenting a wide range of applications that includes the analysis and the manipulation of biological molecules [5], the use of micro-structured reactors and mixers for synthesis processes [6], the generation of droplets or the realization of emulsions [7, 8]. Miniaturized devices offer several advantages including high controllability and precision when handling small volumes of fluid, reduced reagent consumption and a high surface-to-volume ratio [9], thus reducing analysis time and space requirements [10]. The study of flows and transfers occurring in milli-fluidic systems requires access to analytical methods adapted to the size and geometry of the channels as well as the materials used in their fabrication [11]. Optical methods are conventionally and successfully used for high-resolution studies [12], provided that an optical path is accessible, which is not always guaranteed in such systems because the geometry may be complex and the materials may be

Article note: A collection of invited papers based on presentations at the Italian-French International Conference on Magnetic Resonance, Milan, Italy, 27–30 September 2022.

***Corresponding author: Jean-Christophe Perrin**, Université de Lorraine, CNRS, LEMTA, F-54000 Nancy, France, E-mail: jean-christophe.perrin@univ-lorraine.fr
Feryal Guerroudj, Laouès Guendouz and Nicolas Louvet, Université de Lorraine, CNRS, LEMTA, F-54000 Nancy, France
Rainier Hreiz and Jean-Marc Commenge, Université de Lorraine, CNRS, LRGP, F-54000 Nancy, France
Lucie Klopffer, Université de Lorraine, CNRS, LEMTA, F-54000 Nancy, France; and Université de Lorraine, CNRS, LCPME, F-54000 Nancy, France
Laurence Mathieu, Université de Lorraine, CNRS, LCPME, F-54000 Nancy, France; and EPHE, PSL Research University, LCPME, F-54000 Nancy, France

© 2023 IUPAC & De Gruyter. This work is licensed under a Creative Commons Attribution-NonCommercial-NoDerivatives 4.0 International License. For more information, please visit: http://creativecommons.org/licenses/by-nc-nd/4.0/

opaque to light. This is the case with most plastic materials, and in glass, when the wall is curved or too thick (typically >500 μm). In addition, these methods can be invasive (*e.g.* use of tracers that can alter the properties of the fluid) or even destructive (*e.g.* use of lasers in biological systems).

Nuclear magnetic resonance (NMR) methods [13], on the other hand, allow access to opaque media and are able to provide a large amount of physicochemical information [14], as well as to follow phenomena over time in the field of process engineering [15, 16]. For example, NMR and magnetic resonance imaging (MRI) methods have been used to determine the properties of complex fluids [17, 18], to monitor transport phenomena [19] (*e.g.* dispersion and fluid ingress in porous media [20–22], diffusion in electrolyte membranes [23, 24], heat transfer in complex fluids [25, 26], flow of suspensions [27], single or two-phase flows in porous media [28, 29] or flow imaging in micro-fluidic channels [30]) and to characterize electrochemical processes [31, 32]. Due to their low sensitivity, however, NMR/MRI methods may be limited when using standard commercial instruments in cases where sample volume is limited. Efforts for improving the measurement sensitivity are based on different strategies [33], such as increasing the strength of the static magnetic field [34, 35], developing superconducting coils or cryo-probes [36] or using hyperpolarization techniques [37, 38]. Another approach consists in reducing the dimensions of the radiofrequency (RF) coil in order to maximize the filling factor (roughly the fraction between the volume of the sample inside the coil and the sensitive volume of the RF coil) which leads to a higher signal-to-noise ratio (SNR) of the resulting spectrum or image [39–41]. The development of miniaturized RF coils in combination with optimized measurement protocols was shown to be an effective approach for the analysis of small volume samples. Different geometries of miniaturized RF coils have been designed including volumetric (three-dimensional) coils, known for concentrating the RF field at the sample space and for having high filling factors [42]; or planar (two-dimensional) coils, known for their open structure allowing an easy access to the sample space [43, 44]. These specific coils are used and have proved their efficiency in different spectroscopy and imaging studies in chemistry [45], biology [46], high frequencies applications such as electron paramagnetic resonance (EPR) [47] and flow studies in devices handling microliter volumes [48–51].

The realization of such RF coils requires an appropriate sizing and the use of specific microfabrication techniques including 3D printing [52] or etching on rigid substrates such as CuFlon® [53, 54] or on flexible substrates such as polyimide films [55–58].

In this study, specific NMR devices are setup in order to study flows in milli-fluidic systems. Each device includes the RF milli-RF coil adapted to the geometry and the dimensions of the system. The presented development procedure includes the design and the scaling, the electromagnetic simulations of the produced RF field, the fabrication technique and the qualification of the milli-RF coils by comparison with the commercial Brucker MicWB40 probe. The developed methodologies are then applied in two different study cases in milli-fluidics.

Materials and methods

The MRI was performed on a Bruker Avance III 600 WB spectrometer. The superconducting magnet is oriented vertically and generates a static magnetic field B_0 with an intensity of 14.1 T which corresponds to a proton (^1H) Larmor frequency of 600 MHz. The spectrometer is equipped with a gradient imaging system delivering a maximum magnetic field gradient intensity of 150 G/cm.

Fabrication of milli-RF coils on flexible copper/Kapton substrates

The RF coils were fabricated by chemical etching on DuPont™Pyralux®AC copper/Kapton® substrates (Fig. 1). The mask, consisting in a dense black 2D drawing of the milli-RF coil, was first printed on a transparent tracing paper and a photo-sensitive lacquer (Positiv 20 KONTAKT CHEMIE from CRC Industries UK Ltd.) was sprayed on the surface of the substrate (1). The mask, placed on top of the substrate during UV insulation (2), allows a positive transfer of the pattern as the lacquer covering the non-protected zone is fragilized by the UV radiation and is dissolved in the developer product. Only the zone protected by the mask remains (3). The etching was carried out

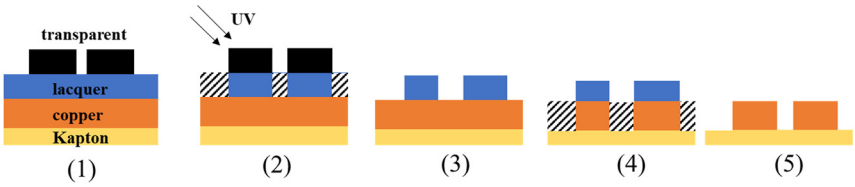

Fig. 1: Etching protocol used for the 2D fabrication of the milli-RF coils.

Table 1: Steps and operating conditions of the etching procedure on the copper/Kapton® substrate.

Thickness of photo-sensitive lacquer	6–8 µm
Copper thickness	45 µm
UV insulation	340 nm < λ_{UV} < 440 nm, exposure time: 1 min. 30 s
Development	Substrate immersed in developer product for 1 min
Etching	Jet of iron perchloride during 1 min. 30 s
Drying	40 °C for 15 min
Tin plating	Etchings immersed in solution of tin plating crystals during 30–60 s

using a jet of iron perchloride, which attacked the unprotected area of the copper until total dissolution (4). Rinsing with ethanol and then water, followed by drying, removed all traces of etching product (5). The resulting etchings were finally immersed in an aqueous solution of tin plating crystals (RS components LTD) to form a protective anti-oxidation layer. The operating conditions considered in each step are summarized in Table 1. This process allowed the fabrication of the milli-RF coils in 2D. The flexibility of the polymer substrate then enabled the 3D realization of the two geometries considered in this work.

Tuning and matching of the electronic circuits

The milli-RF coils were used for both emission and reception. Each milli-RF coil was connected to an electronic circuit composed of capacitors so that the resulting RLC circuit resonated at the proton resonance frequency of 600 MHz (tuning) and its impedance matched the characteristic impedance of the coaxial cable used for the transmission of the generated RF pulses and the received NMR signal (matching).

A commercial Bruker insert designed for a surface coil adapted to our 600 MHz spectrometer was reused by exchanging the coil with the fabricated milli-RF coil. It was then connected to the tuning and matching circuit already present on the insert (Fig. 2(a)) by a coaxial (non-radiating) cable. A pre-tuned circuit was added to complete the tuning (Fig. 2(b)). The commercial circuit consisted of variable capacitors while the pre-tuned circuit consisted of fixed value capacitors, two of which were used for tuning and matching, and a capacitor (C_{sym}) at the "foot" of the coil that allowed a symmetrical AC voltage to be applied to the terminals of the coil (electronic balancing). The values of the fixed capacitors were determined empirically.

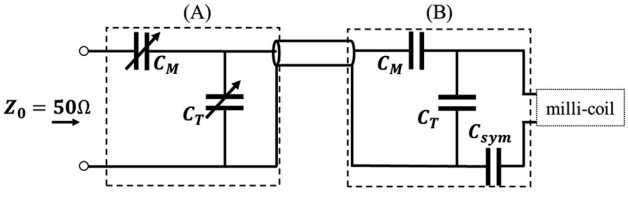

Fig. 2: Electronic circuit for tuning and matching of the milli-RF coils. (a): Circuit of the commercial insert and (b): pre-tuned circuit added.

Electromagnetic simulations

We used a numerical finite element method implemented in COMSOL Multiphysics® to determine the electromagnetic behavior of the RF coils. The method allows to solve the propagation equation of an electromagnetic wave in a restricted domain in order to determine the spatial distribution of the produced field as well as its homogeneity domain. The simulations were performed with the physical interface "Radiofrequency, electromagnetic waves and frequency domain". This interface is used for the calculation of electromagnetic fields and the representation of their distribution in high frequency systems. The parameters considered for the simulations (mesh and calculations) are summarized in Table 2.

Table 2: Considered parameters for electromagnetic simulations under COMSOL Multiphysics®.

properties of the solving domain	Domain	Air sphere
	Electrical conductivity σ	0 S/m
	Relative magnetic permeability μ	1
	Temperature	293.15 K
	Pression	1 atm
	Specification (magnetic isolation)	Dirichlet condition: $n \times E = 0$ (electric field normal to the surface)
Properties of the conductor	Material	Copper
	Relative magnetic permeability μ_r	1
	Relative permittivity ε_r	1
	Electrical conductivity σ	$5.99\ 10^7$ S/m
	Specification (conductive losses on the surface)	Impedance condition at the boundaries (non-perfect conductor)
RF	Transmission cable impedance	50 Ω
	Operating voltage	1 V

Results and discussion

Development and qualification of the milli-RF coils

In this study, the objective is to develop coils adapted to the size and geometry of the considered samples. Thanks to miniaturization, we maximize the filling factor and we anticipate an improvement of the quality of the measurements by an increase of the SNR.

Several factors and constraints determine which geometric design is best suited for each system studied:

- the geometry and dimensions of the system and its placement in the spectrometer;
- the geometrical characteristics of the coils as defined in the literature [39, 59–61];
- factors related to RF, which limit the length of the wires to be used for the realization. In particular, the length l of the conductive wire must correspond substantially to one-tenth of the wavelength ($l \simeq \lambda_{RF}/10 \cong 0.05$ m at 600 MHz). This rule ensures a constant amplitude of the current along the entire length of the wire. Considering these limitations, the two geometric models that have been selected are a Helmholtz milli-RF coil and a saddle milli-RF coil.

The Helmholtz geometry was chosen to perform a hydrodynamics study in an anchor-shaped micromixer. The two loops of the Helmholtz milli-RF coil were placed on either side of the mixing point (*i.e.* the point where the three channels meet) in order to locate velocity field measurements. The dimensions and parameters chosen for this geometry are shown in Fig. 3a.

a)

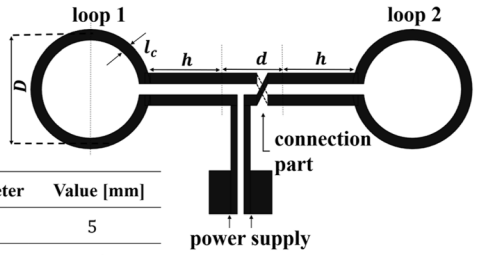

Parameter	Value [mm]
D	5
d	2.5
l_c	0.4
h	3.5

b)

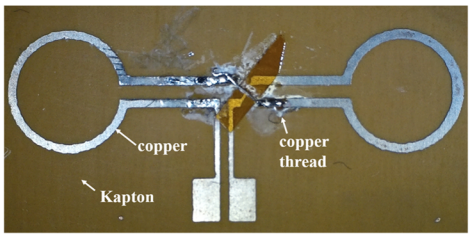

c)

(B) circuit	Value [pF]
C_T	2.7
C_M	1.2
C_{sym}	1.2

d)

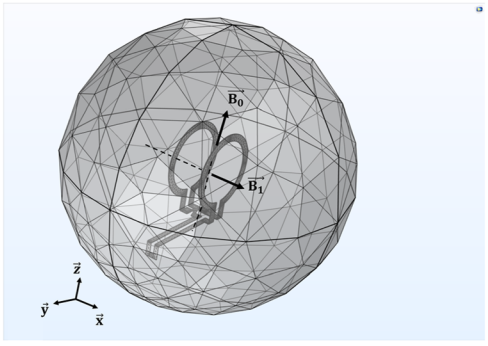

e)

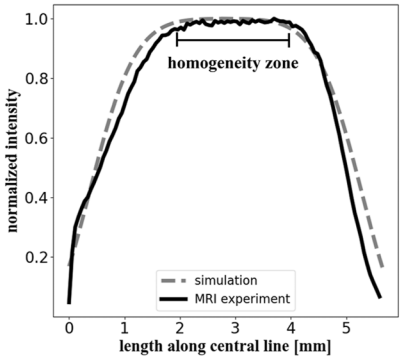

f)

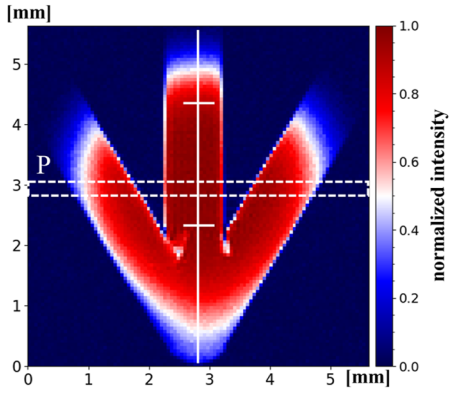

g)

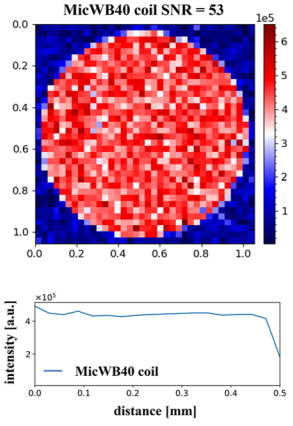

h)

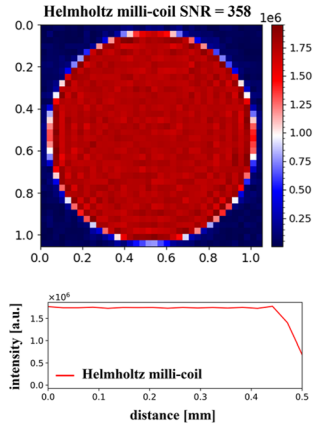

Fig. 3: Development of the Helmholtz milli-RF coil (dimensions and parameters (a), fabrication by etching on copper/Kapton® substrate (b), tuning and matching circuit (c), simulation of the developed model by finite element mesh calculation under COMSOL Multiphysics® (d), plot of normalized intensity profiles over 5.7 mm along the outlet of the micromixer (e), obtained from electromagnetic simulation and from the measurement of a 2D normalized intensity map (f)). Qualification: measurements of 2D NMR signal intensity maps at the P-position using the Brucker MicWB40 coil (g) and the Helmholtz milli-RF coil (h) with their corresponding radial profile plots. Distances on the map axes are in millimeters.

The etching procedure described in Fig. 1 is used with the operating conditions summarized in Table 1 for the realization of the 2D geometry (Fig. 3b), the flexibility of the substrate allowed then the realization of the 3D geometry. The Helmholtz milli-RF coil is connected to the pre-tuned circuit composed of fixed capacitors with the values presented on Fig. 3c.

The simulation of the developed model under COMSOL Multiphysics®, with the parameters summarized on Table 2 and the use of a finite element mesh calculation (Fig. 3d), allowed computing the normalized intensity of the B_1 field produced by the Helmholtz milli-RF coil at 600 MHz over a 5.7 mm distance in the direction of the outlet of the micromixer. The obtained profile (Fig. 3e) shows a plateau that indicates the homogeneity zone of the B_1 field over an estimated length of ~2 mm with a deviation of about 1.5 % from the maximum value.

The fabricated Helmholtz milli-RF coil is used for the measurement of an NMR signal intensity map in a micro-mixer filled with a copper sulfate solution ($CuSO_4$) 0.01 M characterized by a longitudinal relaxation time $T_1 \sim 100$ ms (Fig. 3f). The profile plotted along the central line of the outlet is in good agreement with the simulation result, it also indicates a homogeneous zone of the B_1 field over a length of 2 mm with a deviation of 2 % from the maximum value.

To evaluate the gain in SNR, NMR signal intensity maps are measured in a plane orthogonal to the outlet channel with the Helmholtz milli-RF coil (Fig. 3g) and with the commercial Brucker MicWB40 coil (25 mm ID) (Fig. 3h). Measurements are performed under similar geometrical conditions and with the same acquisition time. The SNR is calculated by dividing the mean value of the NMR signal by its standard deviation. The results show an improvement of the SNR by a factor ~7.

By a similar procedure, we developed a saddle milli-RF coil, chosen for the study of a biofilm development in a capillary ($1 \times 1 \times 100$ mm). The dimensions and the parameters chosen are presented in Fig. 4a. The saddle milli-RF coil was fabricated by the etching procedure described earlier (Fig. 4b) and connected to its pre-tuned circuit (Fig. 4c). The electromagnetic simulation allowed obtaining the profile of the normalized intensity of the B_1 field over a distance of 4.5 mm in the direction of the capillary. The obtained profile indicates a homogeneous B_1 field over a length of 1 mm with a deviation of 2 % from the maximum value (Fig. 4e); this result is in a good agreement with the experimental profile obtained by the MRI measurement of a 2D signal intensity map in a capillary, that also indicates a homogeneous field over 1 mm with a deviation of 3 % from the maximum value.

The Brucker MicWB40 coil is used to measure a 2D signal intensity map (Fig. 4f) and a velocity map (Fig. 4g). The images are compared with the ones recorded in the same conditions using the fabricated saddle milli-RF coil (Fig. 4h and i). The results show an improvement of the SNR on the NMR signal intensity maps by ~17 fold. To evaluate the SNR on the velocity maps, a criteria C was defined as a ratio between the maximum velocity at the center of the section and the standard deviation. The comparison of the obtained values shows an increase of the C criteria by a factor ~9.

The comparison between the measurements performed with the commercial coil and those with each of the developed milli-RF coils showed an improvement of the SNR, thus allowing a detailed analysis of the milli-fluidic phenomena presented in the following applications.

All the acquisition parameters of the MRI images presented in Figs. 3 and 4, as well as those of all the figures in the rest of the article are listed in the Appendix.

Application #1: MRI study of the hydrodynamics in a micromixer

A full description of this study, containing all the details concerning the MRI velocimetry experiments, the numerical simulations and their comparison has been recently published [62]. We will therefore only summarize here the principle of the study and the experimental implementation.

The study consisted in making measurements of the velocity field of a low viscosity liquid (water) along the outlet channel of an arrow-shaped micromixer and comparing the measurements with CFD numerical simulations. This type of mixer is of particular interest because it allows fine control of selectivity in complex competitive syntheses, and thus a reduction in purification costs and energy impact. The objective was to study the hydrodynamic regimes that govern the flow in the mixing channel and that have a strong impact on the quality of the mixture. Indeed, as the mean velocity (and thus the Reynolds number) of the flow increases, the initially stratified flow evolves towards a regular symmetrical vortex flow, which becomes asymmetrical, then periodic and finally unstable, before reaching the laminar-turbulent transition.

a)

Parameter	Value
h_l	4.2 mm
l_l	2.4 mm
l_c	0.4 mm
ϕ	120°
d	2.5 mm

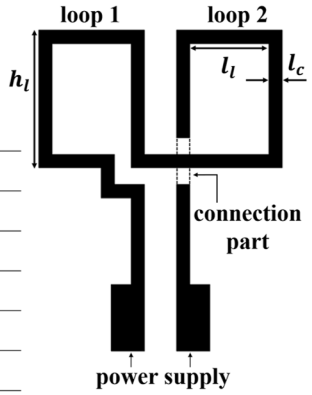

b)

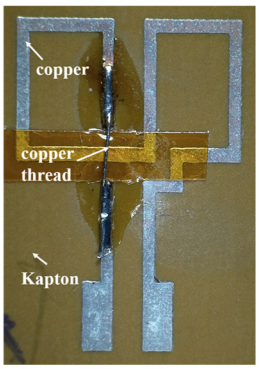

c)

(B) circuit	Value [pF]
C_T	4.7
C_M	1.2
C_{sym}	2.7

d)

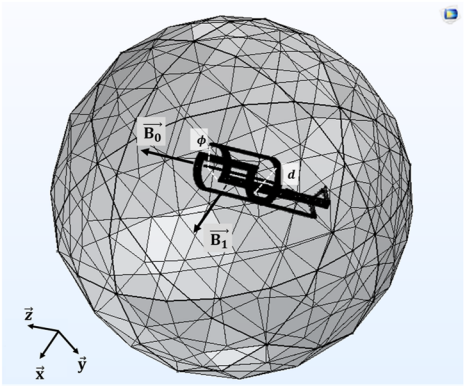

e)

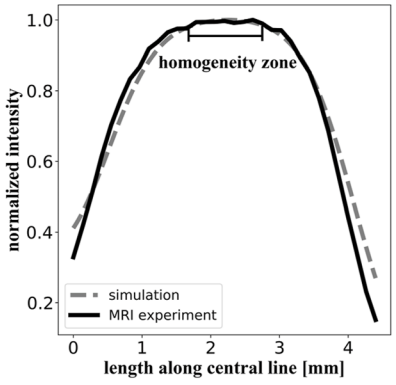

f)

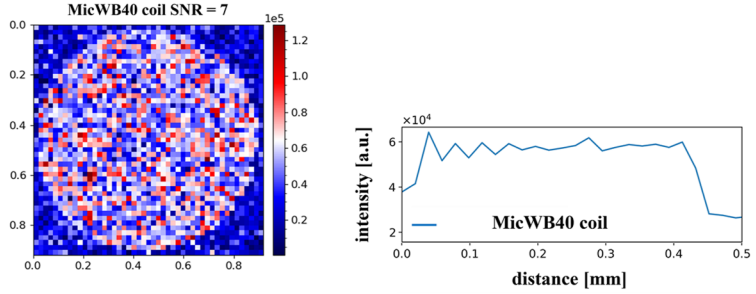

g)

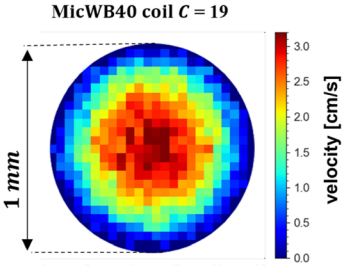

h)

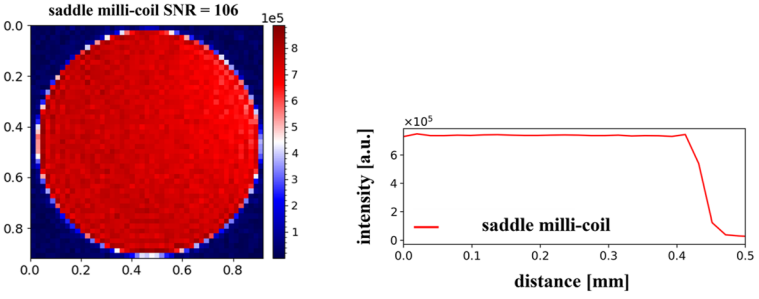

i)

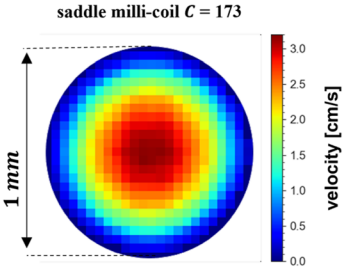

Fig. 4: Development of the saddle milli-RF coil (dimensions and parameters (a), fabrication by etching on copper/Kapton® substrate (b), tuning and matching circuit (c), simulation of the developed model by finite element mesh calculation under COMSOL Multiphysics® (d), plot of normalized intensity profiles along 4.5 mm in the direction of the capillary (e) obtained from electromagnetic simulation and from MRI measurement). Qualification: measurements with the Brucker MicWB40 coil (f, g) and with the saddle milli-RF coil (h, i) of 2D NMR signal intensity maps and velocity maps respectively. Distances on the map axes are in millimeters.

To perform the study, the Helmholtz milli-RF coil discussed in the previous paragraph was integrated into an experimental setup in the 25 mm diameter imaging insert (Fig. 5a and b). Fig. 5c.1 shows an example of water flow velocity maps measured in an axial slice located at the outlet of the micromixer 2.5 mm from the mixing point for an average flow rate per inlet of 1.9 mL/min (Re_{outlet} = 80). The fluids injected into the two inlets were identical (0.01 M $CuSO_4$ solution, $T_1 \sim 100$ ms). The measurement was performed using the commercial microimaging coil. A clockwise rotating vortex is present, with a transverse velocity whose amplitude v_{xy} reaches almost 20 % of the maximum axial velocity. This is much better seen in the maps measured with the fabricated Helmholtz milli-RF coil (Fig. 5c.2). Since the flow conditions and the measurement plane are the same, the same conclusions are drawn, but the images here are of much better quality (increase of the C criteria by a factor ~9). The measurements completely validate the numerical CFD simulation performed in ANSYS Fluent using the exact geometry of the micromixer. The results of the corresponding simulation, whose resolution has been degraded to be identical to that of the MRI experiment, are presented in Fig. 5c.3. The differences between simulation and experiment are hardly visible, both qualitatively and quantitatively. This excellent agreement was verified up to regimes where the average velocity in the output channel reaches ~30 cm/s. Beyond that, the comparison with the simulation highlights the limitations of the imaging protocol used.

Application 2: methodology for MRI visualization of biofilm growth in a capillary tube and its impact on the hydrodynamics of the flow

The second application concerns geothermal energy. Geothermal energy is a renewable energy that has become an important player in the energy mix. The thermal energy of the subsoil is used in heating or air-conditioning installations for individual houses and collective buildings, or for the production of electricity. Aquifers exploited for geothermal applications contain complex microbial ecosystems consisting of various bacterial and archaeal populations interacting with salts, metals and minerals, which evolve through the pore network. During operation, the possible clogging of the porous ground network by biofilms is an important source of fluid circulation problems and the appearance of important pressure losses, which lead to a reduction of efficiency and to the deterioration of the installations.

The biofilms we are interested in are colonies of bacteria growing within a matrix of extracellular polymeric substances and attached to a solid-liquid interface. In the case of aquifers, biofilms generally develop as a layer adherent to the walls of the pores. The detection of the presence of biofilm in a capillary tube thus serves as a prerequisite for the study of the proliferation of bacterial colonies in soils, with the capillary tube serving as a pore model.

In this work we first setup a methodology consisting in growing a bacterial biofilm in a capillary tube of millimetric section. Then we detect its presence via a modification of both the MRI relaxation contrast and the hydrodynamic properties of the flow. The commercial MicWB40 coil is used to have access to a large field of view and to be able to follow the evolution of the growth over time (Fig. 6) while our home-made saddle milli-RF coil is used to measure more finely the local velocity field (Fig. 7).

Biofilm culture protocol

Shewanella oneidensis bacteria are grown in a nutrient medium at 31 °C. The number of bacteria increases exponentially with time to a concentration of approximately 10^9 bact./mL. Conditioning of the capillary surface was performed by circulating the nutrient solution for 1 h 30 min before hosting the bacterial culture. The seeding of the capillary (1 × 1 × 100 mm) was performed under closed-loop circulation of the bacterial culture for 4 h at room temperature. Bacteria retained at the capillary walls are continuously fed with the nutrient medium diluted one-tenth at room temperature. The feed rate imposed by the pump is 1.2 mL/min (corresponding to an average velocity of approximately 2 cm/s in the capillary).

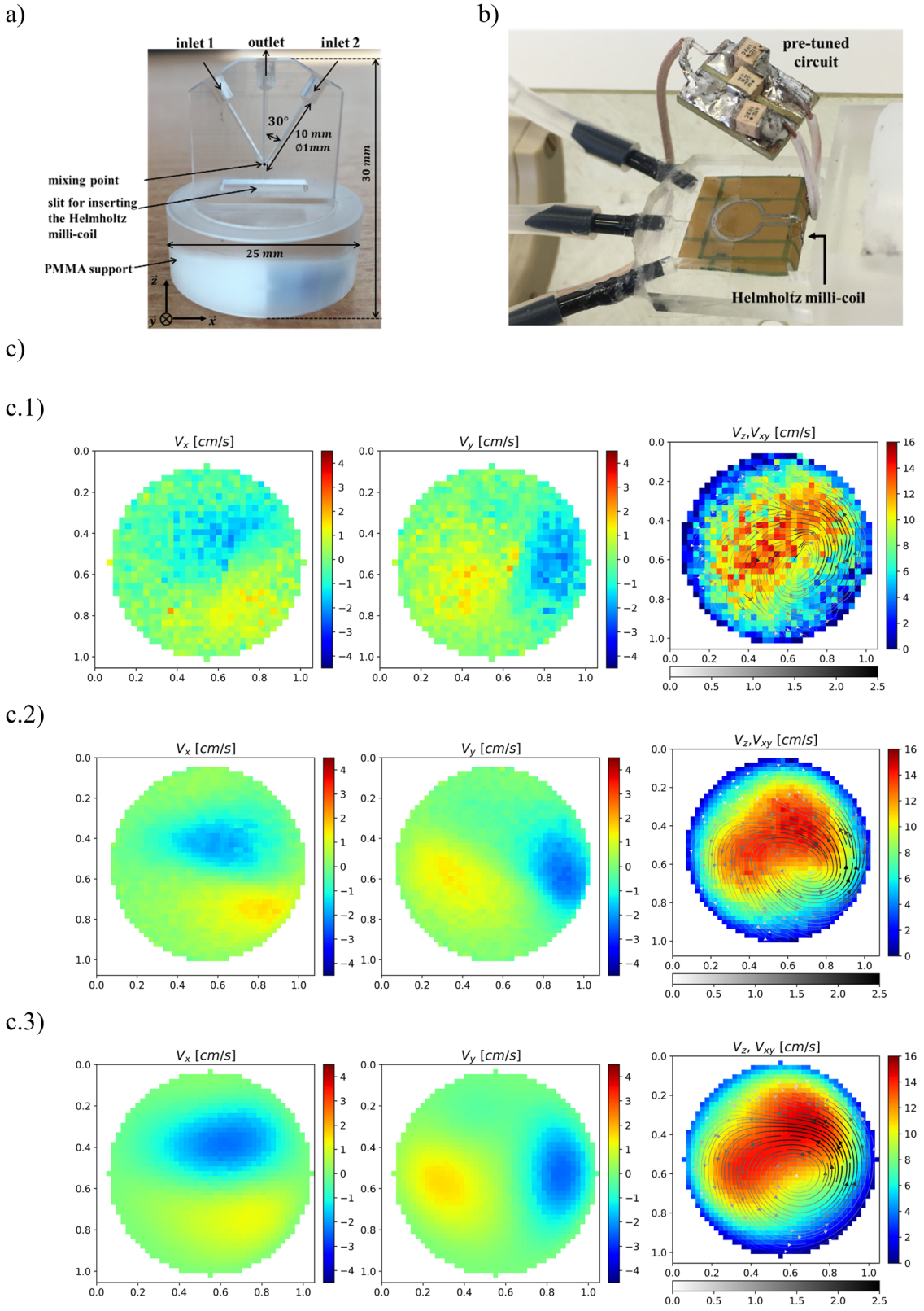

Fig. 5: Velocity components of a water flow in the outlet channel of a micromixer. The flow is characterized by a Reynolds number of 60. (c.1): Measurement realized with the Bruker MicWB40 probe. (c.2): Measurement realized with the home-made milli-RF coil. (c.3): Result of the CFD simulation. The distances on the maps axes are in millimeters.

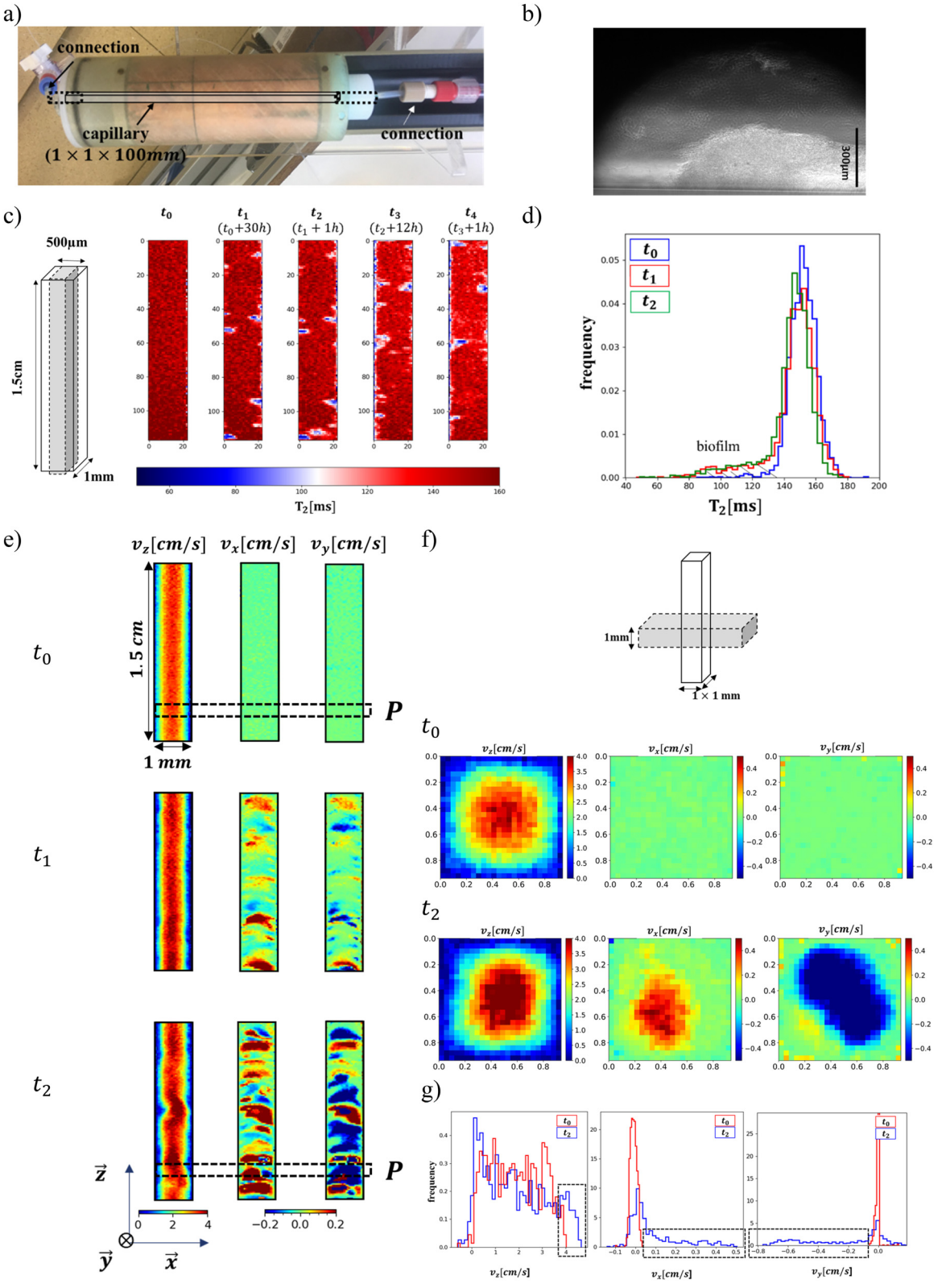

Fig. 6: Monitoring of biofilm growth using optical microscopy (b) and MRI with the commercial probe (a, c, d, e, f, g). The acquisition parameters are listed in the Appendix. Distances on the map axes are in millimeters.

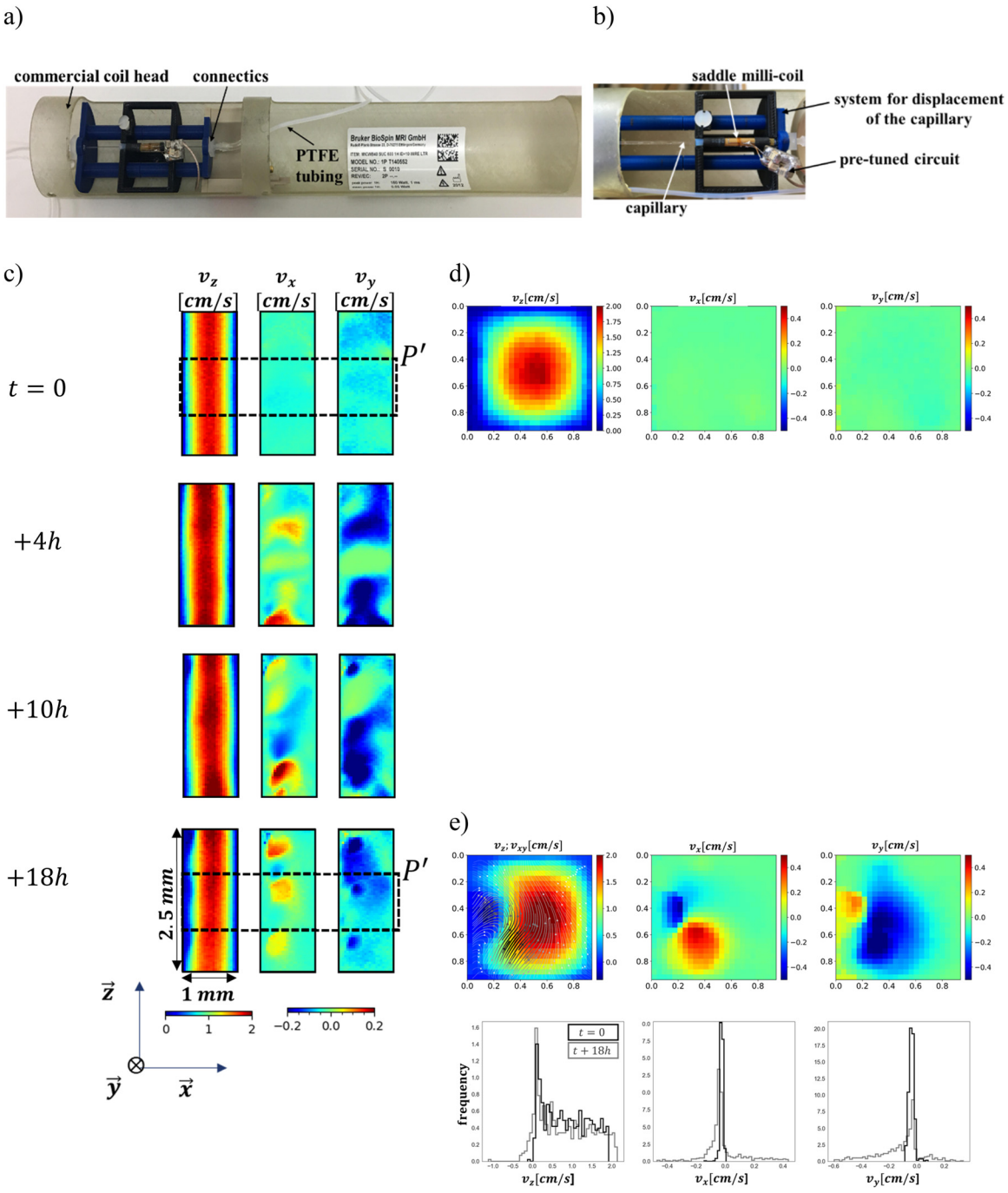

Fig. 7: Visualization of the local 3D velocity field during biofilm growth using the saddle milli-RF coil. The acquisition parameters are listed in the Appendix. Distances on the map axes are in millimeters.

Monitoring of biofilm growth (Fig. 6b–d)

Before performing the NMR experiments, observations were made using an optical microscope. They showed that the biofilm is formed after ~24 h from the beginning of the feeding. The observed structures are thick and distributed along the capillary mainly on the first third from the inlet. These structures develop and occupy the section of the capillary (Fig. 6b). They are not stable/fixed and they sometimes detach when the feeding flow

passes. It has been observed that the feed flow has a dual role: it creates a sheer stress that leads the bacteria to stick to the walls and thus promotes their adhesion, but it then contributes to the detachment of the biofilm when it becomes thicker and reduces the hydraulic section [63, 64]. The flow then transports it and makes it colonize another surface downstream.

This is typically what is observed on the T_2 relaxation time maps (Fig. 6c) where we see clusters of biofilms formed after about 30 h on a capillary length of about 1.5 cm. Some clusters grow slightly over time (t_3) while others disappear, carried away by the flow. The presence of the biofilm is revealed in the images by a significant decrease of the transverse relaxation time from $T_2 \sim 150 \pm 10$ ms for the nutrient solution at t_0 to an averaged value of $T_2 \sim 100 \pm 20$ ms for the protons in the biofilm (Fig. 6d).

Impact of biofilm growth on the 3D velocity field

Maps of the three components of the velocity field in the capillary are first made with the commercial MicWB40 coil using the Flowmap protocol from the Bruker library under Paravision 5.1. Sagittal images are measured with the same geometric parameters as those considered for the relaxation time images in the previous section, and over the same portion of the capillary (Fig. 6e). Axial maps are measured with a resolution of 40×40 μm^2/pixel in a plane located close to the entry of the capillary (Fig. 6f). The velocity field is averaged over a thickness of 1 mm. At time t_0, the measured velocity maps indicate the presence of an axial component v_z corresponding to a Poiseuille flow along the entire visible length of the capillary. The transversal components v_x and v_y both exhibit a narrow distribution centered at 0 (Fig. 6g). As the culture time increases, the velocity profile becomes non-uniform and non-symmetric along the length of the capillary contrary to the rectilinear flow in the clean capillary (Fig. 6e, t_1 and t_2). In areas where biofilm is present, the cross-sectional area is narrowed, resulting in higher axial velocities while secondary flows appear in the transverse plane (Fig. 6f and boxes in Fig. 6g). These secondary flows modify locally the balance of forces and the equilibrium between a mixing regime dominated by diffusion and by advection. The link between the presence of biofilm, the size of the clusters, its spatial distribution on the one hand and the hydrodynamics of the flow on the other hand is therefore particularly important to study in order to better understand how a biofilm grows and how biocide agents might interact with it. Interestingly, and as noted already by Seymour et al. [65], the secondary flows seem to evolve periodically along the capillary axis, with a periodicity that seems here to be close to the dimension of the square section of the capillary tube (1 mm). This periodicity seems to correspond also to the way biofilm clusters are distributed along the capillary (compare Fig. 6c–e at t_2), which would tend to say that the way in which deposition occurs could be related to the lateral size of the capillary. This observation could be important for understanding the growth of biofilms in porous media and should be extended to other capillary sizes and geometries.

More detailed local measurements are then performed using the saddle milli-RF coil. Fig. 7a and b presents the experimental setup. As the homogeneity area of the coil is very small, a displacement system has been realized in order to move the capillary along its axis in the milli-RF coil. As expected, the quality of the velocity maps is clearly improved. The observations made previously with the commercial system are verified. Secondary flows, absent at $t = 0$, are clearly seen from $t = 10$ h and periodic structures are observed again ($t = 18$ h). The axial image in Fig. 7e presents a detailed view of the flow in one of these structures. The v_x and v_y components show alternating signs, demonstrating the presence of a counter-clockwise rotating vortex (see the blacks arrows showing the v_{xy} vector). The axial component v_z also shows negative values, typical of counter-current flows.

Conclusions

In this work we have implemented MRI milli-RF coils adapted to the local measurement of flows containing microliter volumes of liquid. These systems are manufactured at low cost by an etching process on copper/Kapton® substrates. The protocol used includes the dimensioning of the RF coils by simulations of the homogeneity of the produced electromagnetic field, the fabrication, the validation and the implementation in milli-fluidic devices. The fabricated RF coils are more sensitive than the commercial micro-imaging coil – mainly due to a

better filling factor – and are able to characterize precisely and locally the 3D flow field in fluidic systems of millimetric dimensions. The fabricated RF coils have been used in two different cases, to study hydrodynamic instabilities encountered in millimeter-scale mixing processes and to monitor the development of biofilms. These two applications offer interesting perspectives, to help the dimensioning of industrial micromixers and to better control the use of biocides for the remediation of biofilms in geothermal subsoils. Overall, based on the developed method, further technical developments can be implemented and used to study different systems in the field of process and chemical engineering.

Research funding: This study is funded by the French National Research Agency, project BIOCIDES ANR-21-CE50-0027.

Appendix: MRI acquisition parameters

	Fig. 3(f)	**Fig. 3(g) and (h)**
Method	mic_msme	mic_msme
TR	300 ms	300 ms
TE	4.7 ms	5 ms
FOV	1.2×1.2 cm^2	0.75×0.75 cm^2
In-plane resolution	47×47 µm^2/pixel	29×29 µm^2/pixel
Slice thickness	400 µm	200 µm
Slice orientation	Sagittal	Axial
Slice position		2.5 mm from the mixing point
#Accumulations	8	8
Acq. time	10 min	10 min
Solution	Copper sulfate $T_1 \sim 100$ ms	Copper sulfate $T_1 \sim 100$ ms

Fig. 4(f) and (h)		**Fig. 4(g) and (i)**	
Method	mic_msme	Method	Flowmap
TR	500 ms	Protocol	Velocity-map
TE	5.5 ms	TR	500 ms
FOV	0.5×0.5 cm^2	TE	7 ms
In-plane resolution	20×20 µm^2/pixel	Δ	2.88 ms
Slice thickness	500 µm	δ	2.77 ms
Slice orientation	Axial	θ	30°
#Accumulation	1	FOV	0.5×0.5 cm^2
Acq. time	2 min	In-plane resolution	39×39 µm^2
Solution	Copper sulfate $T_1 \sim 100$ ms	Slice thickness	500 µm
		Slice orientation	Axial
		Accumulation	4
		Acq. time	6 min
		Solution	Copper sulfate $T_1 \sim 100$ ms
		Flow rate	0.6 mL/min

Fig. 5(c1) and (c2)			**Fig. 5(c1)**	**Fig. 5(c2)**
Method	Flowmap	Instrumentation	Bruker Micro2.5/MicWB40	Helmholtz milli-RF coil
Protocol	Velocity-map			
TR	300 ms			
TE	6 ms			
Δ	2.16 ms	FOV	1×0.75 cm^2	0.6×0.6 cm^2
δ	2.05 ms			
#Accumulations	4	In-plane resolution	29×29 µm^2	23×23 µm^2
Acq. time	6 min			
(1 Velocity component)				
Solution	Copper sulfate			
Re_{outlet}	80			

(continued)

Fig. 5(c1) and (c2)		Fig. 5(c1)	Fig. 5(c2)
Slice orientation	Axial		
Slice position	2.5 mm		
	From mixing point		
Slice thickness	200 µm		

Figs. 6(c, e and f)	Instrumentation: Bruker Micro2.5/MicWB40
	Fig. 6(c)
Method	MSME
Protocol	MSME-T2-map
TR	15 000 ms
TE_{eff}	15 ms
#Echos	16
#Accumulations	1
Acq. time	24 min
Slice orientation	Sagittal
Slice thickness	500 µm
FOV	0.5×1.5 cm^2
In-plane resolution	40×120 µm^2/pixel

	Fig. 6(e)	**Fig. 6(f)**
Method	Flowmap	Flowmap
Protocol	Velocity-map	Velocity-map
TR	1000 ms	1000 ms
TE	7 ms	7 ms
Δ	2.89 ms	2.89 ms
δ	2.78 ms	2.78 ms
FOV	0.5×1.5 cm^2	0.5×0.5 cm^2
In-plane resolution	40×120µm^2/pixel	40×40 µm^2/pixel
Slice thickness	500 µm	1 mm
Slice orientation	Sagittal	Axial
#Accumulations	4	4
Acq. time	6 min	6 min
(1 Component)		
Flow rate	1.2 mL/min	1.2 mL/min

Fig. 7	Instrumentation: saddle milli-RF coil	
	Fig. 7(c)	Fig. 7(d)
Method	Flowmap	Flowmap
Protocol	Velocity-map	Velocity-map
TR	1000 ms	1000 ms
TE	7 ms	7 ms
Δ	2.89 ms	2.89 ms
δ	2.78 ms	2.78 ms
FOV	0.5×0.5 cm^2	0.5×0.5 cm^2
In-plane resolution	40×40 µm^2/pixel	40×40 µm^2/pixel
Slice thickness	500 µm	1 mm
Slice orientation	Sagittal	Axial
#Accumulations	4	4
Acq. time	6 min	6 min
(1 Component)		
Flow rate	0.6 mL/min	0.6 mL/min

References

[1] L Chen, C Yang, Y Xiao, X Yan, L Hu, M Eggersdorfer, D Chen, D A Weitz, F Ye. *Mater. Today Nano* **16**, 100136 (2021), https://doi.org/10.1016/j.mtnano.2021.100136.

[2] D Figeys, D Pinto. *Anal. Chem.* **72**, 330 A (2000), https://doi.org/10.1021/ac002800y.

[3] A Manz, R C Anderson. *Microsystem Technology in Chemistry and Life Science*, Springer, Berlin Heidelberg (1998).

[4] W Ehrfeld, V Hessel, H Lehr. Microreactors for chemical synthesis and biotechnology—current developments and future applications. In *Microsystem Technology in Chemistry and Life Science Topics in Current Chemistry*, A. Manz, H. Becker (Eds.), Vol. **194**, pp. 233–252, Springer Berlin Heidelberg, Berlin, Heidelberg (1998).

[5] X Chen, D Cui, C Liu, H Li, J Chen. *Anal. Chim. Acta* **584**, 237 (2007), https://doi.org/10.1016/j.aca.2006.11.057.

[6] A J deMello. *Nature* **442**, 394 (2006), https://doi.org/10.1038/nature05062.

[7] A Montillet, S Nedjar, M Tazerout. *Fuel* **106**, 410 (2013), https://doi.org/10.1016/j.fuel.2012.11.018.

[8] C-H Yeh, Y-C Lin. *J. Micromech. Microeng.* **23**, 125025 (2013), https://doi.org/10.1088/0960-1317/23/12/125025.

[9] E Samiei, M Tabrizian, M Hoorfar. *Lab Chip* **16**, 2376 (2016), https://doi.org/10.1039/c6lc00387g.

[10] G M Whitesides. *Nature* **442**, 368 (2006), https://doi.org/10.1038/nature05058.

[11] A Jahanbakhsh, K L Wlodarczyk, D P Hand, R R J Maier, M M Maroto-Valer. *Sensors* **20**, 4030 (2020), https://doi.org/10.3390/s20144030.

[12] R Lindken, M Rossi, S Große, J Westerweel. *Lab Chip* **9**, 2551 (2009), https://doi.org/10.1039/b906558j.

[13] P T Callaghan. *Principles of Nuclear Magnetic Resonance Microscopy*, Clarendon Press, Oxford (1991).

[14] R R Forseth, F C Schroeder. *Curr. Opin. Chem. Biol.* **15** 38, (2011), https://doi.org/10.1016/j.cbpa.2010.10.010.

[15] L F Gladden, P Alexander. *Meas. Sci. Technol.* **7**, 423 (1996), https://doi.org/10.1088/0957-0233/7/3/026.

[16] S Stapf, S-I Han. *NMR Imaging in Chemical Engineering*, John Wiley & Sons Incorporated, Hoboken, Germany (2006).

[17] B Blümich. *NMR Imaging of Materials*, Clarendon Press Oxford University Press, Oxford New York (2000).

[18] P T Callaghan. *Rep. Prog. Phys.* **62**, 599 (1999), https://doi.org/10.1088/0034-4885/62/4/003.

[19] C J Elkins, M T Alley. *Exp. Fluids* **43**, 823 (2007), https://doi.org/10.1007/s00348-007-0383-2.

[20] M Ferrari, J-P Mérel, S Leclerc, C Moyne. *D Stemmelen. diffusion-fundamentals.org* **18**, 1–4 (2013).

[21] J D Seymour, P T Callaghan. *AIChE J.* **43**, 2096 (1997), https://doi.org/10.1002/aic.690430817.

[22] P Mansfield, R Bowtell, S Blackband, D N Guilfoyle. *Magn. Reson. Imaging* **10**, 741 (1992).

[23] A El Kaddouri, J-C Perrin, T Colinart, C Moyne, S Leclerc, L Guendouz, O Lottin. *Macromolecules* **49**, 7296 (2016), https://doi.org/10.1021/acs.macromol.6b01625.

[24]] M Robert, A E Kaddouri, J-C Perrin, S Leclerc, O Lottin. *J. Electrochem. Soc.* **165**, F3209 (2018), https://doi.org/10.1149/2.0231806jes.

[25] M Darbouli, C Métivier, S Leclerc, C Nouar, M Bouteera, D Stemmelen. *Int. J. Heat Mass Transfer* **95**, 742 (2016), https://doi.org/10.1016/j.ijheatmasstransfer.2015.12.056.

[26] S Leclerc, C Métivier. *Exp. Fluids* **59**, 34 (2018), https://doi.org/10.1007/s00348-018-2494-3.

[27] M Jenny, M Ferrari, N Gaudel, S K de Richter. *Europhys. Lett.* **121**, 34003 (2018), https://doi.org/10.1209/0295-5075/121/34003.

[28] J Fannir, S Leclerc, I Panfilova, D Stemmelen. Two-phase displacement. In *Porous Media Studied By MRI Techniques ECMOR XVI – 16th European Conference on the Mathematics of Oil Recovery ECMOR XVI – 16th European Conference on the Mathematics of Oil Recovery*, Barcelona, Spain (2018).

[29] L F Gladden, A J Sederman. *J. Magn. Reson.* **229**, 2 (2013), https://doi.org/10.1016/j.jmr.2012.11.022.

[30] E Harel, A Pines. *J. Magn. Reson.* **193**, 199 (2008), https://doi.org/10.1016/j.jmr.2008.04.037.

[31] K Ogata, E Salager, C J Kerr, A E Fraser, C Ducati, A J Morris, S Hofmann, C P Grey. *Nat. Commun*. **5**, 3217 (2014), https://doi.org/10.1038/ncomms4217.

[32] S-H Cao, S Liu, H-J Sun, L Huang, Z-R Ni, W-L Jiang, M Zhan, Z-Y Zhou, S-G Sun, Z Chen. *Anal. Chem*. **91**, 1686 (2019), https://doi.org/10.1021/acs.analchem.8b04006.

[33] A G Webb. *Anal. Chem.* **84**, 9 (2012), https://doi.org/10.1021/ac201500v.

[34] R Fu, W W Brey, K Shetty, P Gor'kov, S Saha, J R Long, S C Grant, E Y Chekmenev, J Hu, Z Gan, M Sharma, F Zhang, T M Logan, R Brüschweller, A Edison, A Blue, I R Dixon, W D Markiewicz, T A Cross. *J. Magn. Reson.* **177**, 1 (2005), https://doi.org/10.1016/j.jmr.2005.07.013.

[35] V D Schepkin, W W Brey, P L Gor'kov, S C Grant. *Magn. Reson. Imaging* **28**, 400 (2010), https://doi.org/10.1016/j.mri.2009.10.002.

[36] S Junge. Cryogenic and superconducting coils for MRI. In *Encyclopedia of Magnetic Resonance*, R K Harris (Ed.), John Wiley & Sons, Ltd, Chichester, UK (2012).

[37] J H Ardenkjaer-Larsen, B Fridlund, A Gram, G Hansson, L Hansson, M H Lerche, R Servin, M Thaning, K Golman. *Proc. Natl. Acad. Sci.* **100**, 10158 (2003), https://doi.org/10.1073/pnas.1733835100.

[38] C R Bowers, D P Weitekamp. *Phys. Rev. Lett.* **57**, 2645 (1986), https://doi.org/10.1103/physrevlett.57.2645.

[39] D I Hoult, R E Richards. *J. Magn. Reson.* **213**, 329 (2011), https://doi.org/10.1016/j.jmr.2011.09.018.

[40] A G Webb. *Microcoil Nuclear Magnetic Resonance Spectroscopy NMR Spectroscopy in Pharmaceutical Analysis*, p. 48, Department of Bioengineering, Director Huck Institute Magnetic Resonance Centre, Penn State University, University Park, PA, USA (2008).

[41] A G Webb. *J. Magn. Reson.* **229**, 55 (2013), https://doi.org/10.1016/j.jmr.2012.10.004.

[42] A G Webb. *Prog. Nucl. Magn. Reson. Spectrosc.* **31**, 1 (1997), https://doi.org/10.1016/s0079-6565(97)00004-6.

[43] S Eroglu, B Gimi, B Roman, G Friedman, R L Magin. *Concepts Magn. Reson.* **17B**, 1 (2003), https://doi.org/10.1002/cmr.b.10068.
[44] J-C Ginefri, A Rubin, M Tatoulian, M Woytasik, F Boumezbeur, B Djemaï, M Poirier-Quinot, F Lethimonnier, L Darrasse, E Dufour-Gergam. *J. Magn. Reson.* **224**, 61 (2012), https://doi.org/10.1016/j.jmr.2012.09.003.
[45] J N Shoolery. *Prog. Nucl. Magn. Reson. Spectrosc.* **28**, 37 (1995), https://doi.org/10.1016/0079-6565(95)01019-x.
[46] R W Wiseman, T S Moerland, M J Kushmerick. *NMR Biomed.* **6**, 153 (1993), https://doi.org/10.1002/nbm.1940060208.
[47] R Narkowicz, D Suter, R Stonies. *J. Magn. Reson.* **175**, 275 (2005), https://doi.org/10.1016/j.jmr.2005.04.014.
[48] C Massin, F Vincent, A Homsy, K Ehrmann, G Boero, P-A Besse, A Daridon, E Verpoorte, N F de Rooij, R S Popovic. *J. Magn. Reson.* **164**, 242 (2003), https://doi.org/10.1016/s1090-7807(03)00151-4.
[49] E E McDonnell, S Han, C Hilty, K L Pierce, A Pines. *Anal. Chem.* **77**, 8109 (2005), https://doi.org/10.1021/ac051320+.
[50] D L Olson, T L Peck, A G Webb, R L Magin, J V Sweedler. *Science* **270**, 1967 (1995), https://doi.org/10.1126/science.270.5244.1967.
[51] C Massin, G Boero, F Vincent, J Abenhaim, P-A Besse, R S Popovic. *Sens. Actuators, A* **97–98**, 280 (2002), https://doi.org/10.1016/s0924-4247(01)00847-0.
[52] J Xie, X You, Y Huang, Z Ni, X Wang, X Li, C Yang, D Zhang, H Chen, H Sun, Z Chen. *Nat. Commun*. **11**, 5793 (2020), https://doi.org/10.1038/s41467-020-19711-y.
[53] M Klein, J-C Perrin, S Leclerc, L Guendouz, J Dillet, O Lottin. *Macromolecules* **46**, 9259 (2013), https://doi.org/10.1021/ma401511t.
[54] J-C Perrin, C Waldner, J Bossu, A Chatterjee, U Hirn. *Chem. Eng. Sci.* **251**, 117464 (2022), https://doi.org/10.1016/j.ces.2022.117464.
[55] J Dechow, A Forchel, T Lanz, A Haase. *Microelectron. Eng.* **53**, 517 (2000), https://doi.org/10.1016/s0167-9317(00)00368-3.
[56] R C Meier, J Höfflin, V Badilita, U Wallrabe, J G Korvink. *J. Micromech. Microeng.* **24**, 045021 (2014), https://doi.org/10.1088/0960-1317/24/4/045021.
[57] D Murphree, S B Cahn, D Rahmlow, D DeMille. *J. Magn. Reson.* **188**, 160 (2007), https://doi.org/10.1016/j.jmr.2007.05.025.
[58] M Woytasik, J-P Grandchamp, E Dufour-Gergam, J-P Gilles, S Megherbi, E Martincic, H Mathias, P Crozat. *Sens. Actuators, A* **132**, 2 (2006), https://doi.org/10.1016/j.sna.2006.06.062.
[59] A F R Alvarez, E Franco-Mejia, C R Pinedo-Jaramillo. Study and analysis of magnetic field homogeneity of square and circular Helmholtz coil Pairs: a Taylor Series approximation. In *2012 VI Andean Region International Conference 2012 VI Andean Region International Conference*, pp. 77–80, IEEE, Cuenca, Azuay, Ecuador (2012).
[60] D M Ginsberg, M J Melchner. *Rev. Sci. Instrum.* **41**, 122 (1970), https://doi.org/10.1063/1.1684235.
[61] J Wang, S She, S Zhang. *Rev. Sci. Instrum.* **73**, 2175 (2002), https://doi.org/10.1063/1.1471352.
[62] F Guerroudj, R Hreiz, J.-M. Commenge, J Bianchin, C Morlot, T D Le, J.-C Perrin. *Chem. Eng. Sci.* **269**, 118473 (2023), https://doi.org/10.1016/j.ces.2023.118473.
[63] K M Thormann, R M Saville, S Shukla, D A Pelletier, A M Spormann. *J. Bacteriol*. **186**, 8096 (2004), https://doi.org/10.1128/jb.186.23.8096-8104.2004.
[64] K M Thormann, R M Saville, S Shukla, A M Spormann. *J. Bacteriol*. **187**, 1014 (2005), https://doi.org/10.1128/jb.187.3.1014-1021.2005.
[65] J D Seymour, J P Gage, S L Codd, R Gerlach. *Phys. Rev. Lett.* **93**, 198103 (2004), https://doi.org/10.1103/physrevlett.93.198103.